



A technique to select the most obscured galaxy nuclei


Downloaded from: <https://research.chalmers.se>, 2025-12-04 23:25 UTC

Citation for the original published paper (version of record):

Garcia-Bernete, I., Rigopoulou, D., Aalto, S. et al (2022). A technique to select the most obscured galaxy nuclei. *Astronomy and Astrophysics*, 663. <http://dx.doi.org/10.1051/0004-6361/202142749>

N.B. When citing this work, cite the original published paper.

A technique to select the most obscured galaxy nuclei

I. García-Bernete¹ , D. Rigopoulou¹, S. Aalto², H.W.W. Spoon³, A. Hernán-Caballero⁴, A. Efstathiou⁵, P. F. Roche¹, and S. König²

¹ Department of Physics, University of Oxford, Keble Road, Oxford OX1 3RH, UK
 e-mail: igbernete@gmail.com

² Department of Space, Earth and Environment, Onsala Space Observatory, Chalmers University of Technology, 439 92 Onsala, Sweden

³ Cornell Center for Astrophysics and Planetary Science (CCAPS), Department of Astronomy, Cornell University, Ithaca, NY 14853, USA

⁴ Centro de Estudios de Física del Cosmos de Aragón, Plaza San Juan, 1, 44001 Teruel, Spain

⁵ School of Sciences, European University Cyprus, Diogenes street, Engomi 1516, Nicosia, Cyprus

Received 25 November 2021 / Accepted 25 March 2022

ABSTRACT

Compact obscured nuclei (CONs) are mainly found in local luminous and ultraluminous infrared galaxies (U/LIRGs). In the local Universe, these sources are generally selected through the detection of the HCN–vib (3–2) emission line at submillimetre wavelengths. In this work, we present a diagnostic method to select deeply buried nuclei based on mid-infrared (mid-IR) polycyclic aromatic hydrocarbons (PAHs) and mid-IR continuum ratios. Using *Spitzer* InfraRed Spectrograph (IRS) spectra of a representative sample of local ULIRGs ($z < 0.27$), we examine their PAH and underlying continuum emission ratios. For deeply embedded sources, we find that the 9.7 μm silicate absorption band has a particularly pronounced effect on the 11.3 μm PAH feature. The low flux level in the nuclear silicate absorption band enhances the 11.3 μm PAH feature contrast (high PAH equivalent width) compared to that of the other PAH features. The technique has been extended to include the use of the underlying 11.3/12.7 and 11.3/6.2 μm continuum ratios. However, the latter are affected by the extinction coming from both the host galaxy and the nuclear region, whereas the foreground (host-galaxy) extinction is cancelled out when using the PAH equivalent width ratios. We apply our method to local U/LIRGs from the HERUS and GOALS samples and classify 14 ULIRGs and 10 LIRGs as CON candidates, which corresponds to 30% of the ULIRGs and 7% of the LIRGs from these samples. We find that the observed continuum ratios of CON-dominated sources can be explained by assuming torus models with a tapered disc geometry and a smooth dust distribution. This suggests that the nuclear dusty structure of deeply obscured galaxy nuclei has an extremely high dust coverage. Finally, we demonstrate that the use of mid-IR colour–colour diagrams is an effective way to select CON-dominated sources at different redshifts. In particular, the combination of filters of the *James Webb* Space Telescope/Mid-Infrared Instrument will enable the selection of CONs out to $z \sim 1.5$. This will allow the selection of CONs to be extended to high redshifts where U/LIRGs are more numerous.

Key words. galaxies: nuclei – galaxies: ISM – infrared: galaxies – techniques: spectroscopic

1. Introduction

Recent submillimetre (submm) observations revealed the presence of compact (few tens of parsecs) and highly obscured nuclei ($N_{\text{H}} > 10^{25} \text{ cm}^{-2}$) in local luminous ($10^{11} < L_{\text{IR}} < 10^{12} L_{\odot}$, LIRGs) and ultraluminous ($L_{\text{IR}} > 10^{12} L_{\odot}$, ULIRGs) infrared galaxies (e.g., Aalto et al. 2015 and references therein). These compact obscured nuclei (CONs) are considered to be an important phase of galaxy evolution (e.g., Aalto et al. 2015), but because of the high obscuration, the nature of the nuclear embedded source is unclear: it may be an accreting supermassive black hole (SMBH) in an active galactic nucleus (AGN), a nuclear starburst, or a combination of both (e.g., Veilleux et al. 2009). Regardless of the exact nature of the underlying source, studying the properties of CONs enables us to better understand growth processes in galaxies as well as to investigate the relation between black hole mass and spheroid growth (e.g., Kormendy & Ho 2013).

The extremely high extinction associated with the large column densities of gas and dust present in the inner regions of these sources impede their detection at many wavelengths (e.g.,

optical/X-ray). Earlier studies routinely used the 9.7 μm silicate absorption band (e.g., Imanishi et al. 2007; Levenson et al. 2007; Sajina et al. 2007, 2009; Spoon et al. 2007; Sirocky et al. 2008; Georgantopoulos et al. 2011) and mid-IR colours (e.g., Stern et al. 2012; Mateos et al. 2013) for selecting heavily obscured sources. The high column densities of dust produce large optical depths in the 9.7 μm silicate absorption band (e.g., Ossenkopf et al. 1992). The dusty core absorbs a significant fraction of the intrinsic radiation and reprocesses it to emerge at longer wavelengths in the IR. In particular, it has been found that IR emission of deeply buried U/LIRGs can be modelled by assuming dust surrounding the nuclear source with an additional contribution from a starburst and a spheroidal host (see e.g., Herrero-Illana et al. 2017; Marshall et al. 2018; Efstathiou et al. 2021 and references therein).

More recent works found that the HCN (3–2) line in its vibrationally excited $v_2=1$ state (HCN–vib) is an excellent tracer of CONs (e.g., Sakamoto et al. 2010; Imanishi & Nakanishi 2013; Aalto et al. 2015, 2019; Falstad et al. 2021). In particular, Falstad et al. (2021) suggested that a high HCN–vib surface brightness ($\Sigma_{\text{HCN–vib}} > 1 L_{\odot} \text{ pc}^{-2}$ and/or $L_{\text{HCN–vib}}/L_{\text{IR}} > 10^{-8}$)

Table 1. Sources in common between the HERUS and GOALS samples and the CONquest sample.

| Type of source (1) | HERUS (2) | GOALS (3) |
|-----------------------|--------------|--------------|
| ULIRGs | 7/8 | 8/8 |
| LIRGs | 0/19 | 18/19 |
| subLIRGs | 0/19 | 0/19 |

Notes. We note that the denominators correspond to ULIRGs, LIRGs, and subLIRGs that are part of the CONquest sample.

indicates that the core may be optically thick up to submm wavelengths (see also e.g., Sakamoto et al. 2013, 2017; Scoville et al. 2017; Aalto et al. 2019). Using the HCN–vib molecular gas transition, previous studies revealed that 20%–40% of the U/LIRGs in the local Universe harbour previously undetected CONs (e.g., Sakamoto et al. 2010; Imanishi & Nakanishi 2013; Aalto et al. 2015, 2019; Falstad et al. 2021). In particular, Falstad et al. (2021) reported that CONs are more frequently found in ULIRGs (~38%) than in LIRGs (~21%) based on a volume-limited sample of 46 far-IR luminous galaxies ($L_{\text{FIR}(40-400\mu\text{m})} > 10^{10} L_{\odot}$). However, more studies using larger samples are needed to confirm whether or not this is a commonly occurring feature in U/LIRGs, its dependence on luminosity, and/or other properties of the host galaxy.

Polycyclic aromatic hydrocarbon (PAH) features are ubiquitous in a variety of astrophysical objects and environments (see e.g., Li 2020 for a review). PAH molecules absorb ultraviolet (UV)/optical photons resulting in their excitation. The excited molecules emit mid-IR photons via vibrational relaxation (e.g., Leger & Puget 1984; Allamandola et al. 1989). PAHs are likely responsible for the family of strong IR emission bands (3.3, 6.2, 7.7, 8.6, 11.3 and 12.7 μm ; e.g., Tielens 2008) observed in galactic and extragalactic sources. PAH emission features are very prominent in the mid-IR spectra of U/LIRGs (e.g., Lutz et al. 1998; Rigopoulou et al. 1999; Hernán-Caballero & Hatziminaoglou 2011). These molecules absorb a significant fraction of UV and optical photons (mainly) from young stars (e.g., Peeters et al. 2004) and are therefore excellent tracers of the star formation activity in galaxies near and far (e.g., Rigopoulou et al. 1999; Peeters et al. 2004; Brandl et al. 2006; Smith et al. 2007; Farrah et al. 2008; Pope et al. 2008; Hernán-Caballero et al. 2009; Shipley et al. 2016).

PAH emission has also been detected in the IR spectra of CONs (e.g., Falstad et al. 2021) using the relatively large aperture afforded by *Spitzer* (~4"). However, for the archetypal CON NGC 4418, the 11.3 μm feature was not detected in its subarcsecond angular resolution ground-based mid-IR spectrum (Roche et al. 2015). These authors also found a deeper silicate absorption band (i.e. lower flux level of the nuclear silicate absorption band minimum) compared to that measured in the total *Spitzer*/IRS spectrum. This suggests that in deeply embedded sources, the bulk of the observed PAH emission originates primarily in their circumnuclear regions and is therefore likely to experience substantially lower levels of extinction compared to the compact core.

In this work, we use the Infrared Database of Extragalactic Observables from *Spitzer* (IDEOS database; Hernán-Caballero et al. 2016, 2020; Spoon et al. 2022) and archival *Spitzer* IR spectral data of a representative sample of

local U/LIRGs to investigate the impact of the nuclear 9.7 μm silicate absorption on their galaxy-integrated PAH emission. The paper is organised as follows: In Sects. 2 and 3 we describe the sample selection and observations used in this study, respectively. The main results of the PAH emission are presented in Sect. 4. A new diagnostic diagram for selecting deeply buried nuclei is discussed in Sect. 5. In Sect. 6, we discuss the ability of *James Webb* Space Telescope (JWST) mid-IR instrument (MIRI) imager to isolate deeply obscured nuclei. Finally, in Sect. 7, we summarise the main conclusions of this work.

2. The samples

We select a representative sample of local ULIRGs starting from the *HERschel* Ultra Luminous Infrared Galaxy Survey (HERUS; Farrah et al. 2013), which were observed with the *Herschel* Space Observatory (Pilbratt et al. 2010) in spectroscopy and photometry mode. Although not strictly flux limited, we chose the HERUS sample because it includes nearly all ULIRGs at $z < 0.27$ with 60 μm fluxes between 1.7 and 6 Jy. The sample consists of the 42 most luminous ULIRGs in the local Universe, which were also observed by the *Spitzer*/Infrared Spectrograph (IRS; Houck et al. 2004). We refer the reader to Farrah et al. (2013) and Pearson et al. (2016) for further details on the sample.

Although our main focus is on ULIRGs, to sample a wide range of IR luminosities, we also included LIRGs. To do so, we use the LIRGs sample from the Great Observatories All-sky LIRG Survey (GOALS; Armus et al. 2009). The GOALS sample consists of a complete subset of the Infrared Astronomical Satellite (IRAS) Revised Bright Galaxy Sample (RBGS; Sanders et al. 2003) encompassing 179 LIRGs and 22 ULIRGs, which cover different interaction stages and nuclear spectral types. We note that 18 of the 22 ULIRGs in the GOALS sample are common to the HERUS sample. Thus, the combination of the HERUS and GOALS samples leaves a final sample of 179 LIRGs and 46 ULIRGs.

Finally, for the present study, we also use a sample of far-IR luminous galaxies that include CONs (CON-quest sample; Falstad et al. 2021). Although there is a significant overlap between the U/LIRGs present in the CON-quest sample and the samples previously described (see Table 1), we use the CON-quest sample for the sole purpose of testing the effectiveness of the technique for selecting CON sources. We note that Falstad et al. (2021) classified only a fraction of the CON-quest sample as CON sources (i.e. ~38% of the ULIRGs and ~21% of the LIRGs) based on their high HCN–vib surface brightness (see Falstad et al. 2021 for further details).

3. Literature data

The samples described above were cross-correlated with the *Spitzer* Heritage Archive (SHA)¹ in order to select only those with *Spitzer* IRS staring mode observations. In particular, we use the low-resolution ($R \sim 60$ –120) IRS modules: Short-Low (SL1; 7.4–14.5 μm , SL2; 5.2–7.7 μm) and Long-Low (LL1; 19.5–38.0 μm , LL2; 14.0–21.3 μm).

For those galaxies, we retrieve 6.2, 11.3, and 12.7 μm PAH and continuum measurements, and 9.7 μm silicate strengths from the IDEOS database (Spoon et al. 2022). The IDEOS spectra were drawn from the Cornell Atlas of *Spitzer*/IRS Source

¹ <https://sha.ipac.caltech.edu/applications/Spitzer/SHA/>

(CASSIS, version LR7; [Lebouteiller et al. 2011](#)). The IDEOS database includes all the spectra from CASSIS for galaxies beyond the Local Group. The spectra were reduced with the CASSIS software using optimal extraction and tapered column extraction depending on the spatial extent of the source (see [Lebouteiller et al. 2011](#)). We note that a small scaling factor must be applied in order to stitch together the different *Spitzer*/IRS modules. The SL spectrum is scaled to get a smooth stitch between SL and LL modules (see [Hernán-Caballero et al. 2016](#) for a full description of the automated stitching routine used in IDEOS).

A full description of the methods used to obtain the IDEOS measurements is presented in [Hernán-Caballero et al. \(2016, 2020\)](#) and [Spoon et al. \(2022\)](#). In summary, PAH fluxes and equivalent widths (EWs) are measured in different spectral ranges using a combination of polynomial continua, Pearson type-IV distribution profiles for the 6.2, 11.3, and 12.7 μm PAH features and Gaussian profiles for the weaker PAH bands, fine-structure, and H_2 emission lines. The models used also consider attenuation due to the presence of water ices in the 6.2 μm PAH band region. We note that the model described above is not used for measuring 7.7 and 8.6 μm PAHs because of the difficulty in determining a local continuum for these features. The silicate strength is computed as $S_{\text{SiI}} = \ln(f_{\text{peak}}/f_{\text{cont}})$, where f_{peak} corresponds to the peak of the emission or absorption silicate feature and f_{cont} is the flux of the underlying continuum measured at the wavelength of the peak. For the underlying continuum, IDEOS uses either a spline or power-law interpolation between anchor points on both sides of the silicate feature (see [Spoon et al. 2022](#) for details).

4. The mid-infrared emission of highly obscured dusty galaxies

Regardless of the exact nature of the hidden power source, [Sirocky et al. \(2008\)](#) found that when the obscuration is sufficiently high, the radiation emitted by the central source (massive star, AGN and/or starburst nucleus) has a negligible effect on the spectral shape of the emerging IR emission from the surrounding dusty shell. Although PAH emission has been detected in the nuclear region of AGN using subarcsecond-resolution data (e.g., [Hönig et al. 2010](#); [Alonso-Herrero et al. 2014, 2016](#); [Esquej et al. 2014](#); [Jensen et al. 2017](#)), the nuclear PAH emission can be relatively weak compared with that of the circumnuclear regions because of the potential destruction of PAH molecules by the hard radiation field of the nuclear source (e.g., [Roche et al. 1991](#); [Voit 1992](#); [Siebenmorgen et al. 2004](#)). However, shielding of PAH molecules by molecular hydrogen (H_2) is also possible in these regions (e.g., [Rigopoulou et al. 2002](#); [Alonso-Herrero et al. 2014, 2020](#)).

Recently, [Efstathiou et al. \(2021\)](#) modelled the IR emission of local ULIRGs using the HERUS sample and found that the spheroidal host galaxy component significantly contributes to their PAH emission. The same result was also found for LIRGs ([Herrero-Illana et al. 2017](#)). Furthermore, it has also been found that the bulk of the observed PAH emission in deeply embedded sources originates mainly in their circumnuclear regions using *Spitzer* data (e.g., [Marshall et al. 2018](#) and references therein) and also subarcsecond-resolution spectra (e.g., [Alonso-Herrero et al. 2014](#)). Therefore, the bulk of the PAH emission observed in the mid-IR spectrum of a galaxy containing a CON is considered relatively unobscured and is probably excited by young and hot stars (e.g., [Peeters et al. 2004](#)), and/or old stars when present (e.g., [Kaneda et al. 2008](#)). Figure 1

shows a schematic of the view of a galaxy containing a CON as described above, which is represented by a nucleus within an optically thick, centrally heated dust shell surrounded by a host galaxy disc (see also e.g., [Imanishi et al. 2007](#)). We note that throughout this work we use the term circumnuclear PAH emission to refer to the PAH emission of the host galaxy disc, which is significantly less obscured than the PAH emission originating from the compact nuclear region.

4.1. PAH and continuum emission

The impact of the mid-IR continuum on the circumnuclear PAH emission of U/LIRGs was subsequently investigated with *Spitzer*/IRS spectra through the use of the EW of the 6.2 μm PAH feature (see e.g., [Armus et al. 2007](#); [Desai et al. 2007](#); [Spoon et al. 2007](#); [Imanishi et al. 2007](#); [Marshall et al. 2018](#)). Taking into account the spatial scales probed by *Spitzer*/IRS ($\sim 4''$), its resolution element includes emission from many star-forming regions, and in several cases the whole emission of the galaxy. Consequently, PAH emission from U/LIRGs as measured by *Spitzer*/IRS is averaged over large areas of the galaxies and the PAH ratios measured from each source are expected to be roughly similar.

Using a sample of local star-forming galaxies, [Hernán-Caballero et al. \(2020\)](#) found a strong correlation between the 12.7/11.3 μm PAH flux ratio and the 9.7 μm silicate strength. These authors showed that the PAH EW ratio of the 12.7 and 11.2 μm PAH bands is independent of the optical depth with only a small dispersion ($\sim 5\%$), suggesting that star-forming galaxies have a nearly constant intrinsic PAH flux ratio.

To investigate the relation between PAH emission and obscuration in local ULIRGs, we plot the 12.7/11.3 μm PAH EW ratio versus the silicate strength using *Spitzer*/IRS data for the HERUS sample (see left panel of Fig. 2). We find that a group of ULIRGs, hereafter group 1 (green-coloured stars), shows 12.7/11.3 μm PAH EW ratios similar to those found by [Hernán-Caballero et al. \(2020\)](#) for star-forming galaxies (3σ ; dashed black lines in left panel of Fig. 2). The remaining ULIRGs can be found in two groups, one below (group 2, blue-coloured circles) and the other above (group 3, red-coloured squares) the range occupied by star-forming galaxies (in our case group 1 of ULIRGs).

To further investigate the differences between the spectral features for these groups of ULIRGs, we construct the average spectra of each group using only those galaxies with firm PAH detections (i.e. we do not include those with upper limits). To do so, first we correct the spectra to the rest-frame of each source and we resample them with the same wavelength grid. We then normalise each spectrum at 20 μm (which is a featureless part of the continuum) and finally we average the spectra of the various groups (see Fig. 3).

It is instructive to take a closer look at the values seen in group 2 of ULIRGs. These tend to cluster around low values of the 12.7/11.3 μm PAH EW ratios (average value of ~ 0.2 ; solid blue line in the left panel of Fig. 2) which are more than 3σ below the mean value for star-forming galaxies. We also find that group 2 of ULIRGs follow the 12.7/11.3 μm PAH flux ratio versus silicate strength relation but with an offset relative to star-forming galaxies presented in [Hernán-Caballero et al. \(2020\)](#) (see right panel of Fig. 2). This indicates that, in group 2 of ULIRGs, the silicate strength measured by *Spitzer*/IRS is deeper than expected from the 12.7/11.3 μm PAH flux ratio versus silicate strength relation found for normal galaxies (see Fig. 3). Under the assumption that the circumnuclear star-forming regions of ULIRGs have similar averaged 12.7/11.3 μm

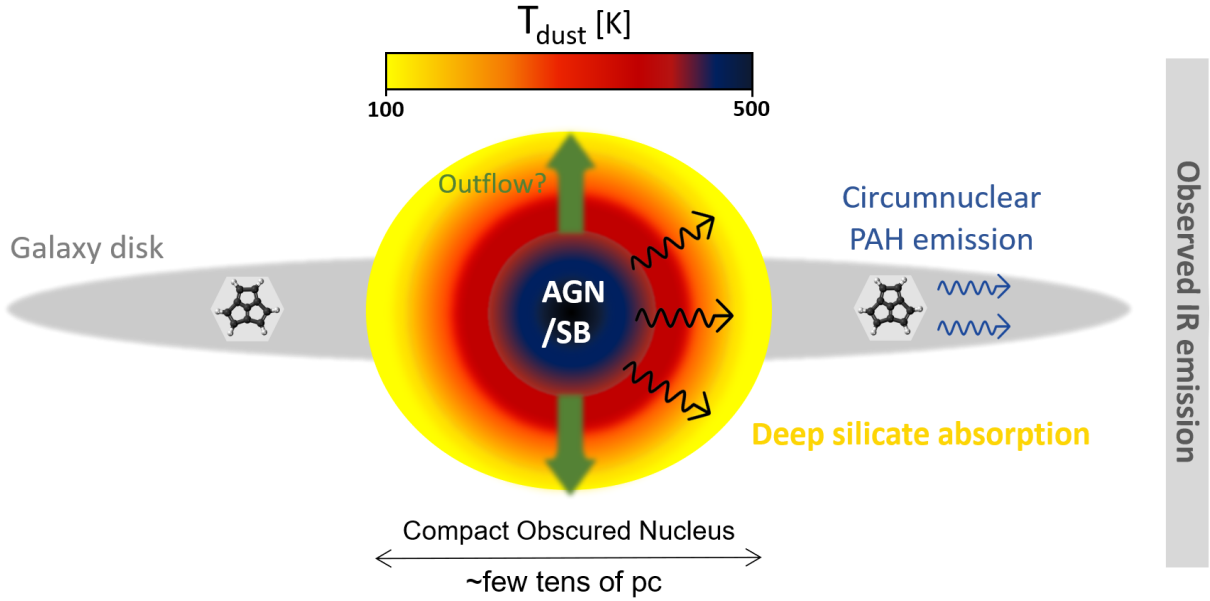


Fig. 1. Schematic view of a galaxy containing a CON (not to scale). The cartoon depicts a compact obscured nucleus, with its submillimetre HCN–vib emission emerging from inside the inner few tens of parsecs (Aalto et al. 2015) surrounded by a star-formation galaxy disc where PAH molecules mainly reside. The total IR emission of a CON galaxy includes contributions from two distinct components: one coming from a heavily obscured nucleus (with a deep $9.7\,\mu\text{m}$ silicate absorption) and the other from the host galaxy disc (circumnuclear PAH emission). The colour scheme used represents the dust temperature gradient of the CON ranging from black (high values) to yellow (lower values of the dust temperature). The green vertical arrows represent the existence of possible outflows whose presence has been confirmed in some CON sources (e.g., Falstad et al. 2019 and references therein) suggesting that the geometry of the compact obscured nucleus may not be perfectly spherically symmetric. The grey shaded rectangle on the right side of the plot (labelled ‘observed IR emission’) represents the large aperture of *Spitzer*/IRS which contains a significant part of the total IR flux of the galaxy. We note that the fraction of the galaxy included in the *Spitzer*/IRS aperture depends on the size of the slit with respect to the size of the galaxy and its distance (see Appendix A). See also Fig. 5 for further details on the total IR emission of galaxies containing CONs.

intrinsic PAH flux ratios compared to those of star-forming galaxies, the offset found in group 2 of ULIRGs (described above) is consistent with an additional continuum component with very deep silicate absorption. However, group 3 of ULIRGs show a greater dispersion in the PAH EW ratios than those of groups 1 and 2.

We find that the majority of ULIRGs within group 3 correspond to sources dominated by unobscured AGN (see red squares in Fig. 4). Indeed, the sources in group 3 show weak silicate absorption or moderate silicate emission (see Figs. 2 and 3), which indicates moderate to no obscuration of the nuclear mid-IR emission (i.e. a significant fraction of nuclear emission escapes through the nuclear obscurer along a viewing angle without being absorbed). As a result, the observed galaxy integrated silicate strength of group 3 of ULIRGs indicates the contribution of nuclear AGN spectrum (with silicate emission) and circumnuclear PAH emission with moderate extinction. Although sources dominated by unobscured AGN show different PAH ratios, in obscured AGN the average PAH ratios measured within the *Spitzer*/IRS aperture are not different from those of star-forming galaxies (see e.g., García-Bernete et al. 2022 and references therein). Finally, in Appendix A we estimate the fraction of the galaxy integrated mid-IR emission that is measured by *Spitzer*/IRS for the various groups of sources described above. We conclude that the fraction of the galaxy observed by *Spitzer*/IRS is not driving the classification of the sources used in this work.

In deeply embedded sources, the nuclear dusty structure and the main source of the circumnuclear PAH emission observed in the total *Spitzer*/IRS spectra are likely to be located in different

physical regions and therefore suffer different degrees of extinction. The EW indicates the strength of a feature compared to its underlying continuum. Therefore, assuming that the galaxy-integrated PAH ratios measured from each source are roughly the same (see e.g., Hernán-Caballero et al. 2020), any differences in the PAH EW ratios are likely not related to the emission from the circumnuclear region of U/LIRGs but rather reflect differences in the continuum that is coming from the nuclear source (see e.g., Imanishi et al. 2007). As expected, we find an anti-correlation between PAH EW and continuum ratios, indicating that the PAH EW ratio is tracing the underlying continuum emission. We therefore suggest that the intrinsic shape of the IR nuclear continuum is the driving force behind the differences in the PAH EW ratios between the two groups of ULIRGs (group 1 and 2).

This idea is demonstrated in Fig. 5 where we generate the IR spectra of galaxies containing CONs using two template spectra: the first is from NGC 4418, a galaxy whose SED is dominated by a very deep silicate absorption feature (black solid line, representing the nuclear CON) and the other is the host galaxy template from Marshall et al. (2018), a circumnuclear PAH spectrum (green solid line representing the host galaxy providing the circumnuclear emission). By varying the contribution of the host galaxy spectrum (from dark red to blue corresponding to increasing values of the host galaxy contribution) with respect to the nuclear source we show the possible range of mid-IR spectra of the CONs. Figure 5 illustrates how the effect of the deep $9.7\,\mu\text{m}$ silicate absorption feature present in CONs is particularly pronounced in their $11.3\,\mu\text{m}$ PAH feature. The low flux level of the nuclear silicate absorption band enhances the $11.3\,\mu\text{m}$ PAH

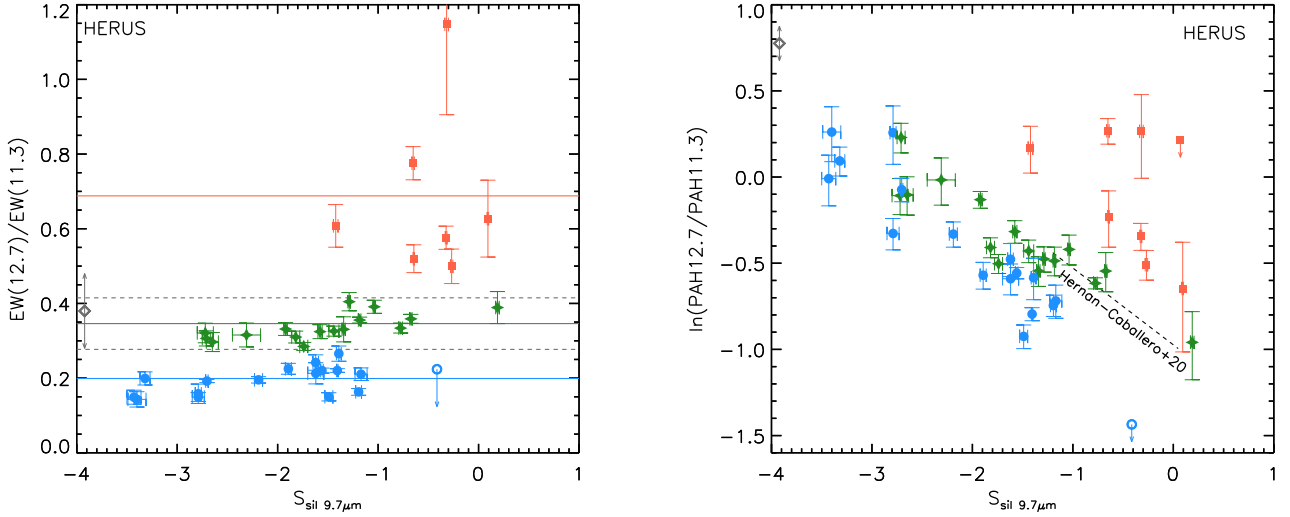


Fig. 2. Dependence of the PAH EW and flux ratios with the silicate strength. Left panel: 12.7/11.3 μm PAH EW ratio versus the strength of the 9.7 μm silicate feature for the HERUS sample. The grey solid and dashed horizontal lines correspond to the average and 3σ values found by [Hernán-Caballero et al. \(2020\)](#) for star-forming galaxies. The blue and red solid horizontal lines represent the average values found for groups 2 and 3 of ULIRGs (see text). Right panel: Same as the left panel but using the 12.7/11.3 μm PAH flux ratio instead of the PAH EW ratio. Green stars, blue circles, and red squares correspond to groups 1, 2, and 3 of ULIRGs (see text). The black dashed line represents the correlation result from the fit of star-forming galaxies ([Hernán-Caballero et al. 2020](#)). Open blue circles and open grey diamonds correspond to sources with PAH EW upper limits. The silicate strength is computed as $S_{\text{sil}} = \ln(f_{\text{peak}}/f_{\text{cont}})$ (see Sect. 3).

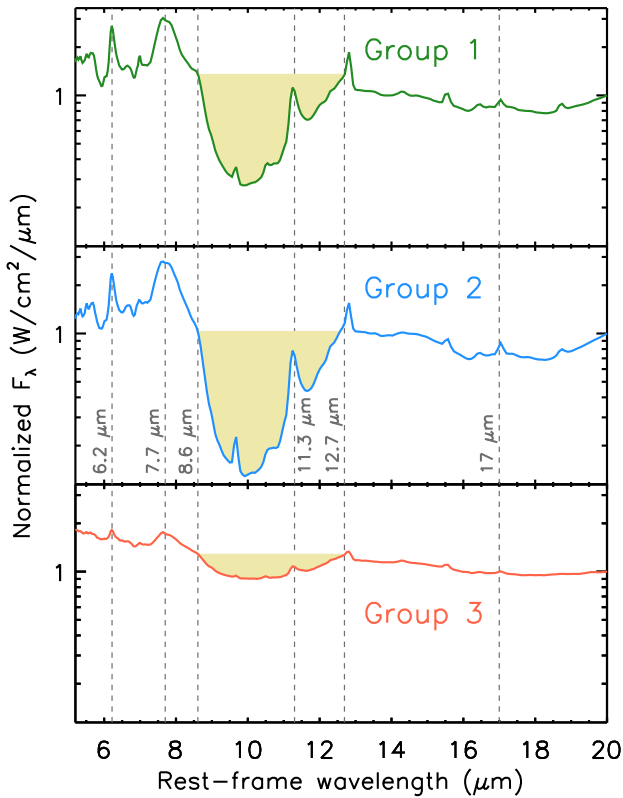


Fig. 3. Average spectra (normalized at 20 μm) for the three ULIRG groups defined in Sect. 4.1. The grey vertical dashed lines denote the location of the strongest PAH bands (6.2, 7.7, 8.6, 11.3, 12.7 and 17 μm). The yellow shaded region highlights the different degrees of silicate absorptions for the various ULIRG groups.

feature contrast (high PAH EW) compared to that of other PAH features. Consequently, the levels of dilution of the 12.7 μm (and 6.2 μm) PAH bands by the nuclear continuum is high compared

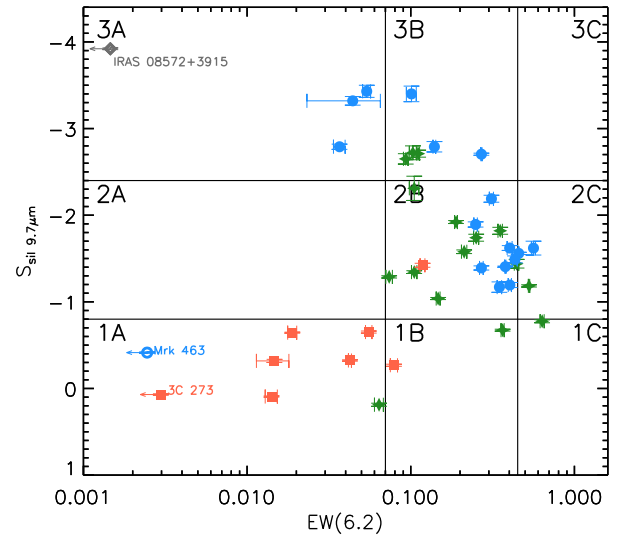


Fig. 4. ‘Fork’ diagnostic diagram ([Spoon et al. 2007](#)) using the 6.2 μm PAH EW width versus the strength of the 9.7 μm silicate feature for the HERUS sample. The colour symbols are the same as in Fig. 2.

to that at 11.3 μm because of the shape of the intrinsic continuum SED of the heavily obscured nucleus.

The left panel of Fig. 6 shows the 12.7/11.3 μm PAH EW ratio versus the 11.3 μm PAH EW for the HERUS sample. For comparison, we also plot the CON-quest sample which includes confirmed CON sources (these are the labelled sources in the right panel of Fig. 6). We note that there are seven sources in common between the HERUS and CON-quest samples (see Sect. 2). However, it is worth clarifying that we only use the CON-quest sample to compare the trends observed in group 2 of ULIRGs with those of confirmed CON sources.

In general, the 12.7/11.3 μm PAH EW ratios of CON sources are below the 3σ values found in star-forming galaxies (grey dashed line). In particular, for a given 11.3 μm PAH, CON

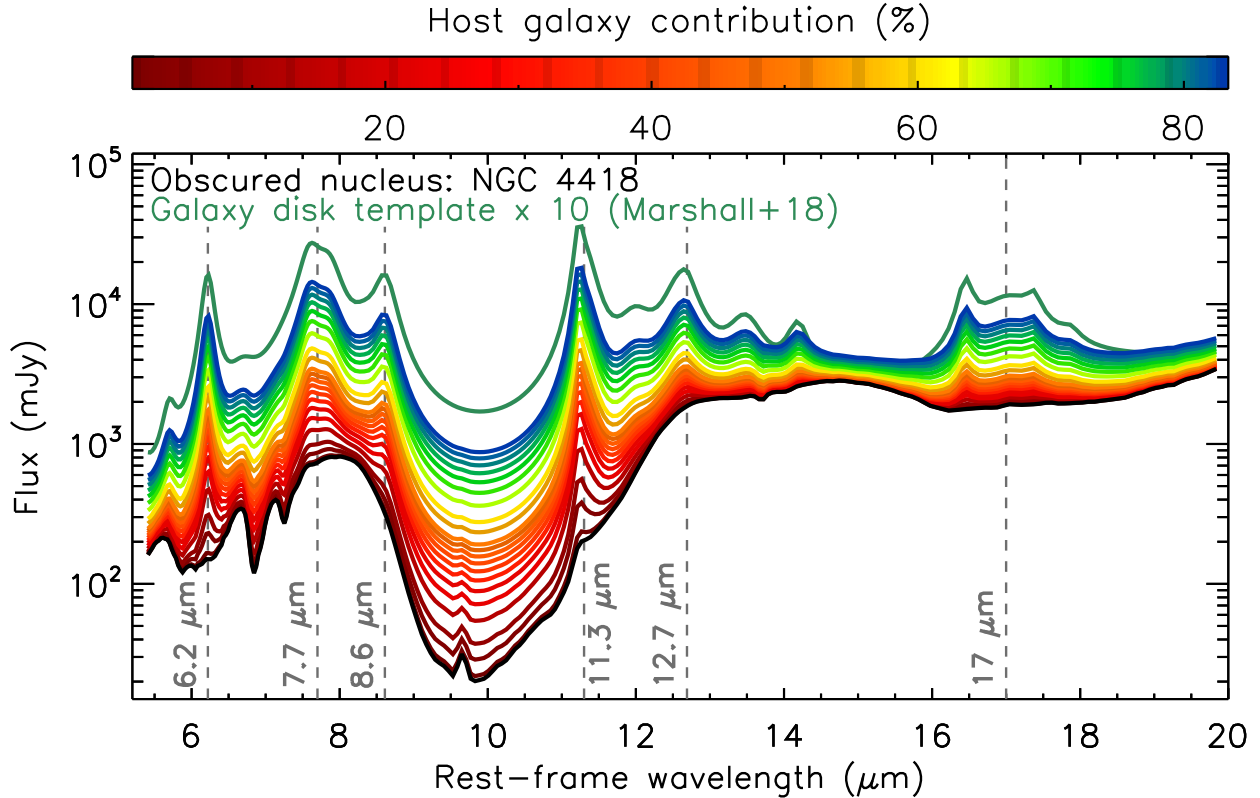


Fig. 5. Predicted range of mid-IR spectra of galaxies containing a CON. These spectra are generated using different fractions of the host galaxy (represented by the host galaxy disc template from [Marshall et al. 2018](#); solid green line) superimposed on the *Spitzer*/IRS spectrum of the archetypical CON-dominated source NGC 4418 (black solid line). The colour-code represents different fractions of the host galaxy. Dark red to blue solid lines correspond to increasing values of the host galaxy contribution with respect to the nuclear source. The grey vertical dashed lines denote the location of the strongest PAH bands (6.2, 7.7, 8.6, 11.3, 12.7 and 17 μm).

sources tend to have low 12.7/11.3 μm PAH EW ratios (dotted green lines). From this plot, it is clear that the degree of dilution of the 11.3 and 12.7 μm PAH features is different between galaxies harbouring deeply obscured nuclei and those of normal star-forming galaxies.

4.2. Comparisons with other dusty galaxies

To further investigate the properties of ULIRGs in group 2, which likely include galaxies with heavily obscured nuclei, we focus first on the sample of far-IR luminous galaxies that include confirmed compact obscured nuclei (CON-quest sample; [Falstad et al. 2021](#)). For this purpose, we plot the 12.7/11.3 μm PAH EW ratio and silicate strength of the CON-quest sample (see Fig. 7). We find that the majority of the sources classified as CONs in [Falstad et al. \(2021\)](#) show small values of the 12.7/11.3 μm PAH EW ratio similar to what we found earlier for ULIRGs in group 2.

However, for both CONs and group 2 of ULIRGs, we find a large range in the values of the silicate strength measured by *Spitzer*/IRS ($\sim 4''$). [Levenson et al. \(2007\)](#) found that a foreground screen model for the obscuration of the host galaxy cannot reproduce the 9.7 μm silicate absorption band observed in the mid-IR spectra of some ULIRGs. Given the *Spitzer*/IRS resolution element for our sources, the observed 9.7 μm silicate absorption band consists of a combination of various components from different physical regions. We note that any contribution from extended structures within the relatively large aperture of *Spitzer*/IRS can result in the filling of the silicate absorption feature (e.g., [Levenson et al. 2007](#);

[González-Martín et al. 2013](#); [Hatziminaoglou et al. 2015](#)). [Roche et al. \(2015\)](#) also found a higher flux level in the silicate minimum measured by *Spitzer*/IRS compared to that measured in the subarcsecond angular resolution, mid-IR, ground-based spectrum of the archetypical CON galaxy NGC 4418. However, the high-angular-resolution spectrum of NGC 4418 shows the same continuum flux level as the *Spitzer*/IRS spectrum in the range $\sim 11\text{--}13\mu\text{m}$ (see Fig. 1 in [Roche et al. 2015](#)). This indicates that the mid-IR slope of the continuum ($\sim 11\text{--}13\mu\text{m}$) is likely tracing the shape of the nuclear silicate absorption band in the integrated IR spectra of the deeply obscured nucleus NGC 4418.

In summary, our findings suggest that the 12.7/11.3 μm PAH EW ratio (and the 11.3/12.7 μm mid-IR continuum ratio) enables us to select ULIRGs with a deep nuclear silicate absorption band even in the relatively large aperture probed by *Spitzer*.

5. A new diagnostic diagram for selecting deeply obscured galaxy nuclei

So far, the detection of the HCN–vib line has shown to be an effective method to confirm the existence of deeply obscured nuclei in local galaxies (e.g., [Sakamoto et al. 2010](#); [Imanishi & Nakanishi 2013](#); [Aalto et al. 2015, 2019](#); [Falstad et al. 2019, 2021](#)). However, detecting CONs at high redshifts is challenging because of the faintness of the HCN–vib line. Here we investigate whether or not the impact of the 9.7 μm silicate absorption on the PAH EW ratios can provide a reliable alternative method for unveiling deeply obscured galaxy nuclei.

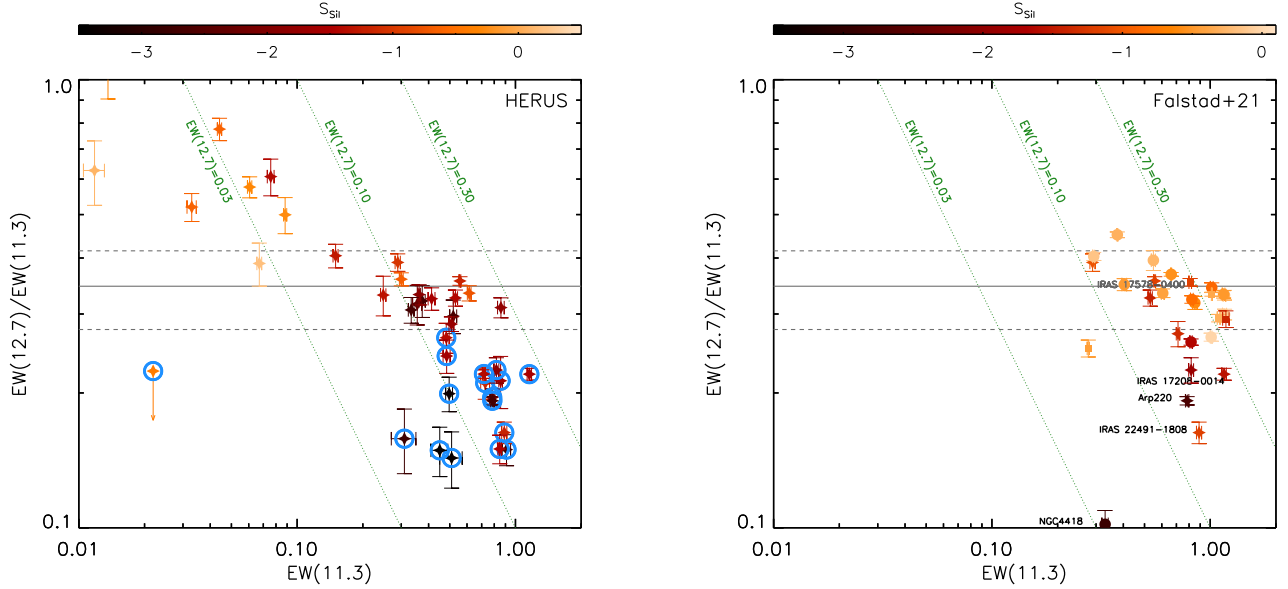


Fig. 6. 12.7/11.3 μm PAH EW ratio versus PAH EW(11.3). *Left panel:* EW plot for the HERUS sample. Open blue circles correspond to group of 2 ULIRGs. *Right panel:* EW plot for the CON-quest sample. Labelled sources correspond to those galaxies classified as CONs in Falstad et al. (2021). Colour-coded stars, circles, and squares represent the strength of the 9.7 μm silicate feature of ULIRGs, LIRGs, and subLIRGs, respectively. Colour-coded symbols correspond to the strength of the 9.7 μm silicate feature. The grey solid and dashed horizontal lines correspond to the average and 3σ values found by Hernán-Caballero et al. (2020) for star-forming galaxies. Finally, the green dotted lines represent constant values of the 12.7 μm PAH EW (0.03, 0.10 and 0.30).

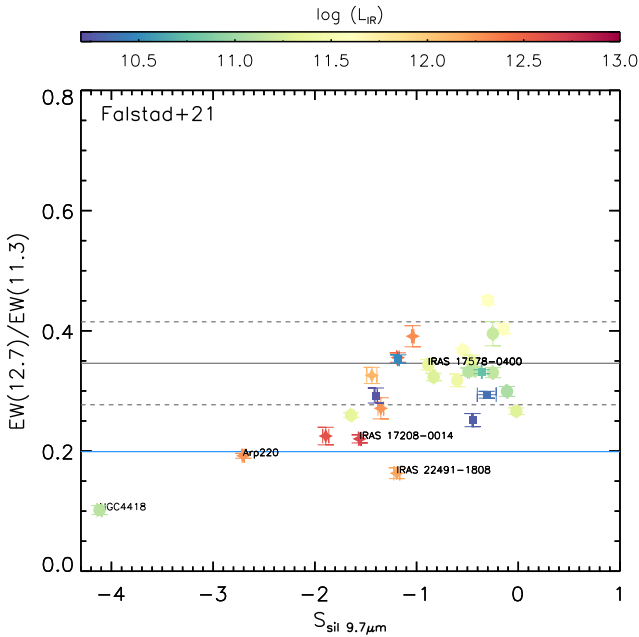


Fig. 7. Same as Fig. 2 but for the CON-quest sample. Labelled sources correspond to same galaxies as in Fig. 6 (i.e. those galaxies classified as CONs in Falstad et al. 2021). Colour-coded stars, circles, and squares represent the IR luminosity of ULIRGs, LIRGs, and subLIRGs, respectively. The grey solid and dashed horizontal lines correspond to the average and 3σ values found by Hernán-Caballero et al. (2020) for star-forming galaxies. Blue solid line corresponds to average value found for group 2 of ULIRGs (see text).

In Sect. 4.1, we show that the 12.7/11.3 μm PAH EW ratios of sources with a deeply buried nucleus are different from those of normal star-forming galaxies (see Fig. 7). Furthermore, we find that the CON classification does not depend strongly on the

silicate strength measured by *Spitzer*. This is because emission from the host galaxy can easily fill the silicate feature as measured by *Spitzer*/IRS (even if its contribution is relatively small; see Fig. 5). Due to the relatively low angular resolution afforded by *Spitzer*/IRS, we expect some degree of contribution from the host galaxy to the total mid-IR spectra. Therefore, the integrated galaxy silicate strength alone is not a good indicator of deeply buried nuclei.

We therefore explored whether or not various PAH EW ratios and mid-IR continuum ratios could enable us to identify deeply buried nuclei. The 6.2/11.3 μm PAH EW ratio is driven by the different levels of dilution by the nuclear continuum (see Sect. 4.1). However, it is worth noting that the broad water ice absorption band peaking at $\sim 6.0 \mu\text{m}$ can affect the 6.2 μm PAH flux if it is not properly included in the mid-IR models (e.g., Spoon et al. 2007). In that case, the value of the EW(6.2) will increase as the continuum gets depressed by the water ice band (assuming the same intrinsic 6.2 μm PAH flux). To mitigate this effect, the EW(6.2) values employed in our work have been corrected for the 6 μm ice absorption band (IDEOS database). It is also worth noting that the water ice absorption band is always weaker than the silicate absorption feature in embedded sources (see e.g., Boogert et al. 2008, 2011 for buried young stellar objects inside dense molecular clouds). Therefore, deeply buried nuclei are expected to have small values of the 6.2/11.3 μm PAH EW ratio compared to normal star-forming galaxies (see Sect. 4.1).

In addition, taking into account the geometry assumed in Fig. 1 for a galaxy containing a CON, the ices would cover the dusty nuclear sources and the bulk of the PAH emission would reside beyond that region. Therefore, any foreground emission will result in filling of the ice absorption feature and, consequently, any fitted ice correction can only be a lower limit on the intrinsic ice absorption band. We note that the black arrows in Fig. 8 indicate the effect the ice absorption correction has on the 6.2/11.3 μm PAH EW ratio.

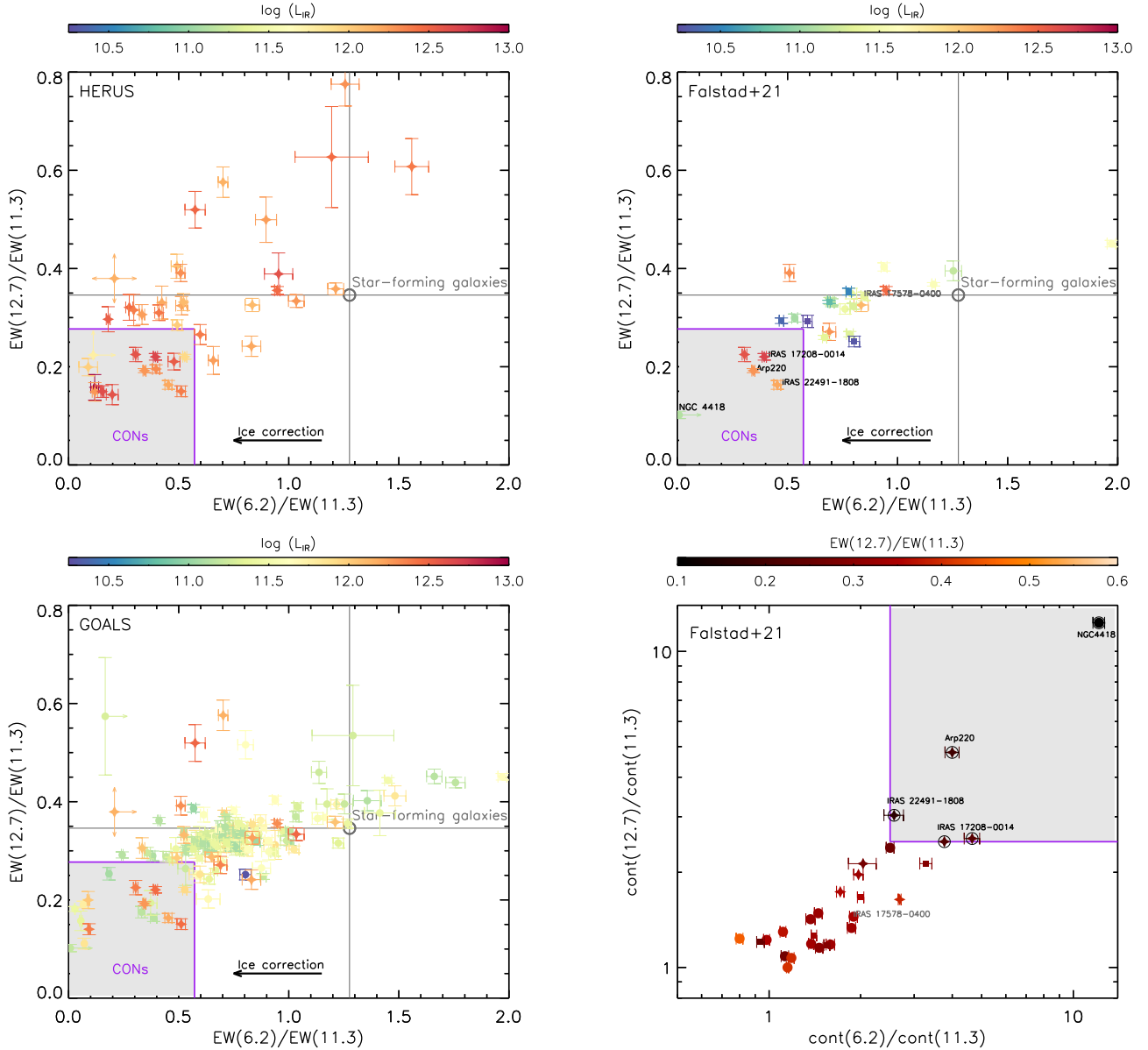


Fig. 8. Diagnostic diagrams for identifying heavily obscured nuclei. *From top left- to bottom right-hand panels:* the HERUS, CON-quest, and GOALS sample. Colour-coded stars, circles, and squares represent the IR luminosity of ULIRGs, LIRGs, and subLIRGs, respectively. The grey solid vertical and horizontal lines correspond to the average values for star-forming galaxies. The black arrows indicate the effect the ice absorption correction has on the 6.2/11.3 μm PAH EW ratio. The purple square denotes the region defined by the PAH $\text{EW}(6.2 \mu\text{m})/\text{EW}(11.3 \mu\text{m}) < 0.572$ and PAH $\text{EW}(12.7 \mu\text{m})/\text{EW}(11.3 \mu\text{m}) < 0.277$ (see text). *Bottom right panel:* diagnostic diagram based on continuum ratios for the CON-quest sample. The purple square denotes the region defined by the continuum flux ratios: $\text{cont}(11.3 \mu\text{m})/\text{cont}(6.2 \mu\text{m}) > 2.5$ and $\text{cont}(11.3 \mu\text{m})/\text{cont}(12.7 \mu\text{m}) > 2.5$ (see text). Colour-coded stars, circles, and squares represent the 12.7/11.3 μm PAH EW ratio of ULIRGs, LIRGs, and subLIRGs, respectively. Open black circles correspond to sources within the purple square in top right panel. Labelled sources correspond to those galaxies classified as CONs in Falstad et al. (2021).

We next compare the 6.2/11.3 versus 12.7/11.3 μm PAH EW ratios of galaxies in the HERUS, CON-quest, and GOALS samples (Fig. 8 from top left- to bottom left-hand panels). The plots reveal that there are marked differences in the PAH EW values of sources containing deeply buried nuclei and those of star-forming galaxies. Using the CON-quest sample as our ‘testbed’ sample for CON sources, our method selects four of the five sources already classified as CONs by Falstad et al. (2021) (or 5 of 6 if we include the prototypical CON IC 860) by using the purple box shown in Fig. 8. To define this box, we use the 3σ value from the average 12.7/11.3 PAH EW and 2σ value from the average 6.2/11.3 PAH EW of the star-forming galaxy sample used in Hernán-Caballero et al.

(2020). We note that two LIRGs classified as CONs by Falstad et al. (2021) (namely Zw 049.057 and ESO 320-G030) are not included in this work because they have not been observed in the *Spitzer*/IRS staring mode. Figure 8 demonstrates how the presence of a heavily obscured nucleus can be unveiled using the PAH $\text{EW}(6.2 \mu\text{m})/\text{EW}(11.3 \mu\text{m}) < 0.572$ and PAH $\text{EW}(12.7 \mu\text{m})/\text{EW}(11.3 \mu\text{m}) < 0.277$ criteria². In essence, what these ratios measure is the different degree of dilution of the 11.3 μm PAH compared with that of the 12.7 μm (and 6.2 μm) PAH due to the silicate absorption feature.

² We note that these criteria can vary depending on the employed method to fit the mid-IR continuum and the dust emission features.

Finally, in order to investigate the existence of deeply obscured nuclei in sources with non-detection in the PAH bands, we introduce an additional diagnostic tool based on the continuum fluxes at 6.2, 11.3, and 12.7 μm (bottom right panel of Fig. 8). Using the CON-quest sample, we confirm that the diagnostic plot based on 11.3/12.7 and 11.3/6.2 μm continuum flux ratios is also capable of identifying CONs. For the continuum ratios, we define the region for selecting CON-candidates by ensuring the selection of the sources classified with the PAH EW criteria. In particular, we use the following continuum flux ratios: $\text{cont}(11.3 \mu\text{m})/\text{cont}(6.2 \mu\text{m}) > 2.5$ and $\text{cont}(11.3 \mu\text{m})/\text{cont}(12.7 \mu\text{m}) > 2.5$ (see the purple box in the bottom right panel of Fig. 8). Although the continuum ratios method can be useful when the 6.2, 11.3, and/or 12.7 μm PAH bands are not detected, the method does present some limitations. The PAH EW ratio allows us to discard sources with deep silicate absorption due to foreground absorbers because they affect both the continuum and circumnuclear PAH emission equally. Thus, the foreground extinction is cancelled out in the PAH EW ratio. However, the continuum ratios are affected by the extinction coming from both the host galaxy and the nuclear region. We note that the former can be the dominant one in edge-on galaxies (e.g., [Goulding et al. 2012](#)).

Identifying CONs using mid-IR spectroscopy. By applying the PAH EW criteria described above, we were able to identify 13 ULIRGs from the HERUS sample, and 10 LIRGs and 8 ULIRGs from the GOALS sample as CON candidates. We note that 7 of the 8 ULIRGs identified as CON candidates are common to both the GOALS and the HERUS samples (see Sect. 2 for more details on the overlap between the two samples). Therefore, our diagnostic method identifies 30% of the ULIRGs and 7% of the LIRGs as CON-candidates from the HERUS and GOALS samples. It is worth noting that our method identifies IRAS 14348-1447 as a CON candidate despite the fact that the galaxy has $\Sigma_{\text{HCN-vib}} < 1 L_{\odot} \text{pc}^{-2}$ and therefore is not formally identified as a CON in [Falstad et al. 2021](#).

The percentage of ULIRGs identified as CON candidates by our method agrees well with those reported by [Falstad et al. \(2021\)](#). However, our method recovers a lower number of LIRG CON candidates than [Falstad et al. \(2021\)](#) (7% vs. 21%). A possible explanation for the lower detection rate of CONs in LIRGs could be the higher levels of contribution from the host galaxy emission to the total mid-IR spectrum as probed by *Spitzer* (see Fig. 5). This is related to the fact that the mid-IR-continuum-emitting regions of LIRGs are not as compact as those in ULIRGs (e.g., [Díaz-Santos et al. 2008, 2010](#); see also Appendix A). Thus, considering the angular resolution of *Spitzer*/IRS ($\sim 4''$), we expect a higher contribution from the host galaxy to the mid-IR spectra of LIRGs. Finally, we find no CON candidate in the subLIRGs sample ($L_{\text{IR}} < 10^{11} L_{\odot}$), in agreement with the results reported by [Falstad et al. \(2021\)](#).

Considering our lower detection rate (i.e. 7%) and taking into account the U/LIRG number density in the local Universe ($\sim 6 \times 10^{-5} \text{Mpc}^{-3}$; [Sanders et al. 2003](#)), we infer a CON density $\geq 4.1 \times 10^{-6} \text{Mpc}^{-3}$ (see also [Falstad et al. 2021](#)). The higher detection rate in ULIRGs can be related to the lower dilution of the CON emission by the host galaxy in highly luminous sources.

Finally, we note that IRAS 17578-0400, which is classified as a CON in [Falstad et al. \(2021\)](#), is not selected by the PAH EW (or continuum) ratios. This LIRG has a highly inclined galaxy disc ($i \sim 80^\circ$), which is part of the interacting system in an early stage of merging ([Stierwalt et al. 2013](#)). Because of the low spa-

tial resolution afforded by *Spitzer*/IRS, together with the fact that LIRGs have relatively extended mid-IR emission, it is likely that the galaxy-integrated mid-IR spectrum of IRAS 17578-0400 is dominated by circumnuclear emission. Thus, higher spatial resolution data is needed to properly isolate the nuclear source. Figure 5 illustrates the impact of the host galaxy contribution to the total IR emission of galaxies containing CONs (see also Sect. 4.2).

6. Prospects for identifying compact obscured nuclei with the *James Webb Space Telescope*

The recent launch of the JWST opens an alternative route to identifying CONs by exploiting the presence of the 9.7 μm silicate absorption and its impact on the IR emission. The unprecedented combination of sensitivity and high spatial resolution in the mid-IR range will allow us to investigate the most distant and faintest galaxies. Therefore, it is of interest to examine the possible use of broad-band JWST filters to unveil compact obscured nuclei in local and high-redshift sources.

To produce a very deep nuclear silicate absorption feature, the dusty structure must be in a centrally heated dust geometry with a temperature gradient and have an extremely high dust coverage (i.e. optical depth) due to cold absorbing material, at least towards our line of sight, because any warm emitting material that has a significantly lower obscuration would result in the filling of the silicate absorption feature (e.g., [Smith et al. 1989](#); [Levenson et al. 2007](#); [González-Martín et al. 2013](#); [Roche et al. 2015](#)). Therefore, torus models with a high covering factor and smooth dust distribution are expected to be well suited to reproducing the observed continuum ratios of deeply obscured galaxy nuclei (see e.g., [Levenson et al. 2007](#)).

In Fig. 9 we compare the observed continuum ratios (12.7/11.3 μm vs. 6.2/11.3 μm) with those obtained from the CYGNUS smooth torus models by [Efstathiou & Rowan-Robinson \(1995\)](#) and [Efstathiou et al. \(2021\)](#). We use the same continuum ratios (i.e. 12.7/11.3 μm vs. 6.2/11.3 μm) as those presented in Sect. 5 (Fig. 8). We find that the observed continuum ratios of CON-dominated sources can be explained by assuming a tapered disc geometry and smooth torus models. This suggests that the nuclear dusty structure of deeply obscured galaxy nuclei has indeed an extremely high dust coverage. In addition, the best-suited torus SEDs for reproducing the observed continuum ratios of CON-dominated sources tend to have relatively high equatorial optical depths ($\tau_{1000\text{Å}}$) and almost edge-on values of the torus inclination angle (see Fig. 9).

In order to test the ability of JWST mid-infrared instrument (MIRI) imager to isolate deeply obscured nuclei, we use the predictions of the smooth CYGNUS torus models (see Fig. 9) and combinations of the various JWST filter transmission curves. F1300W filter mainly tracks the 11.3 μm PAH feature and part of the 9.7 μm silicate band (also F1000W), and F1280W covers the 12.7 μm PAH feature and [Ne II] emission line. F1800W samples the 18 μm silicate band, whereas F1500W, F2100W, and F2500W sample the continuum and weaker features. To select those SEDs that are representative of CON-dominated sources (i.e. relatively low host galaxy contribution) we use the continuum ratio criteria presented in Sect. 5.

In the left panel of Fig. 10 we present a JWST colour-colour diagram based on ratios of the F1130W, F1280W, and F1500W filters. We define a region (purple box) in this diagram for maximising the selection of CON-dominated sources (i.e. $\text{F1280W}/\text{F1130W} > 2.2$ and $\text{F1500W}/\text{F1130W} > 1.6$). Using this

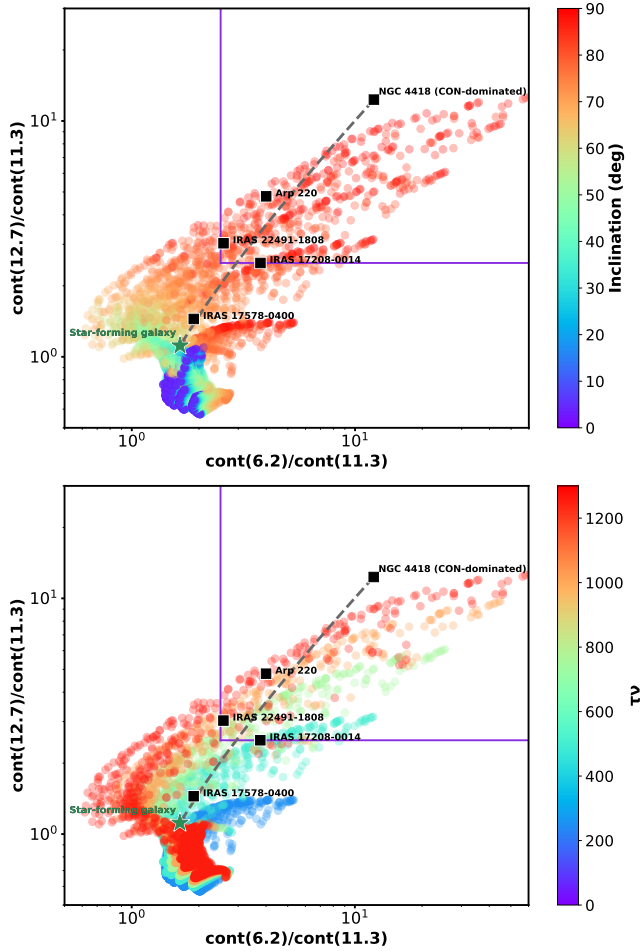


Fig. 9. Comparison of the observed continuum ratios seen in CONs ($12.7/11.3\mu\text{m}$ vs. $6.2/11.3\mu\text{m}$) to those computed from the smooth CYGNUS models by Efstathiou & Rowan-Robinson (1995) and Efstathiou et al. (2021). The black squares correspond to the observed values of the CONs. The green star represents a normal star-forming galaxy. Colour-coded circle symbols represent the torus inclination angle and equatorial optical depth ($\tau_{1000\text{\AA}}$) in the top and bottom panels, respectively. The purple square denotes the region where CON-dominated sources are located and defined by the continuum flux ratios: $\text{cont}(11.3\mu\text{m})/\text{cont}(6.2\mu\text{m}) > 2.5$ and $\text{cont}(11.3\mu\text{m})/\text{cont}(12.7\mu\text{m}) > 2.5$. The dashed grey line corresponds to a track of simulated spectra for galaxies containing a CON varying contributions of the host galaxy as presented in Fig. 5.

diagram at $z = 0$, we recover $\sim 95\%$ of the CONs (i.e. model SEDs representing CON sources) with $\sim 8\%$ contamination from non-CON SEDs. However, even in CON-dominated sources, a small contribution of the host galaxy is expected. Thus, for comparison, we also plot the expected values of the predicted spectra of galaxies containing a CON shown in Fig. 5 (colour squares in Fig. 10). We find that this diagram is effective for host-galaxy contributions to the mid-IR spectrum $\lesssim 50\%$. Similar results are obtained when using combinations of F1000W, F1800W, and F2100W filters. Finally, we investigate the combination of additional JWST filters which will enable us to select CONs at higher redshifts. The right panel of Fig. 10 shows that the F1500W/F2100W–F1500W/1800W diagram is effective at selecting CONs at $z = 1$. Using the latter diagram, we recover $\sim 91\%$ of the CONs (see the purple region in the right panel of Fig. 10; F1500W/F2100W > 10.2 and

F1500W/1800W > 3.9) with $\sim 6\%$ contamination from non-CON SEDs. We find similar results for $z = 0.5$ and 1.5 using the F2100W/F1500W–F1800W/F1500W and F1800W/F2500W–F2100W/F2500W diagrams, respectively. Given the effectiveness of the mid-IR colour–colour diagrams for unveiling CON-dominated sources, JWST will offer a unique opportunity to push the identification of CONs beyond the local Universe. Furthermore, the combination of the high spatial resolution of JWST and its PSF stability will result in minimising the impact of the host galaxy in the measured mid-IR emission of CONs. In a forthcoming paper, we will investigate JWST/MIRI simulations of galaxies containing a CON to further evaluate the ability of JWST to correctly isolate the nuclear emission from the circum-nuclear galaxy emission in these sources.

7. Conclusions

We present a method for identifying compact obscured nuclei that relies on the effect of the silicate absorption band on the EW of the PAH emission. The method was applied to *Spitzer*/IRS spectra of a representative sample of local U/LIRGs. The main results of our study can be summarised as follows.

1. The intrinsic shape of the IR nuclear continuum is the driving force behind the differences in the $6.2/11.3$ and $12.7/11.3\mu\text{m}$ PAH EW ratios in U/LIRGs. We find a strong anticorrelation between the galaxy-integrated PAH EW ratio and the ratio of the underlying continuum of the PAH features.
2. In compact obscured nuclei, we find that the effect of the $9.7\mu\text{m}$ silicate absorption band is particularly pronounced in the EW of the $11.3\mu\text{m}$ PAH feature. The low flux level of the nuclear silicate absorption band enhances the $11.3\mu\text{m}$ PAH feature contrast (high PAH equivalent width) compared to that of the other PAH features (i.e. 6.2 and $12.7\mu\text{m}$ PAH bands).
3. Using the $12.7/11.3\mu\text{m}$ PAH EW ratio (and the $11.3/12.7\mu\text{m}$ mid-IR continuum ratio) we are able to select sources with a deep nuclear silicate absorption band even in the relatively large aperture probed by *Spitzer* ($\sim 4''$).
4. We introduce a method to identify heavily obscured nuclei based on PAH EW ratios. We demonstrate that the use of $\text{PAH EW}(6.2\mu\text{m})/\text{EW}(11.3\mu\text{m}) < 0.572$ and $\text{PAH EW}(12.7\mu\text{m})/\text{EW}(11.3\mu\text{m}) < 0.277$ is able to select CON sources in samples of local U/LIRGs. We note that these criteria can vary depending on the method used to fit the mid-IR continuum and the dust emission features. We extend the technique to the use of the underlying $11.3/12.7$ and $11.3/6.2\mu\text{m}$ continuum ratios: $\text{cont}(11.3\mu\text{m})/\text{cont}(6.2\mu\text{m}) > 2.5$ and $\text{cont}(11.3\mu\text{m})/\text{cont}(12.7\mu\text{m}) > 2.5$. However, we note they these are affected by the extinction coming from both the host galaxy and the nuclear region, whereas the foreground extinction is cancelled out in the PAH EW ratios. Therefore, we suggest that the selection based on continuum ratios should only be used when the 6.2 , 11.3 , and/or $12.7\mu\text{m}$ PAH bands are not detected.
5. Using the PAH EW ratio diagram, we classify 14 ULIRGs and 10 LIRGs from local U/LIRGs samples (i.e. HERUS and GOALS) as CON candidates. We find that our diagnostic method identifies 30% of the ULIRGs and 7% of the LIRGs as CON candidates from these samples combined. Using the lower detection rate, we infer a CON density $\gtrsim 4.1 \times 10^{-6} \text{ Mpc}^{-3}$.
6. The observed continuum ratios of CON-dominated sources can be matched assuming torus models with a tapered disc

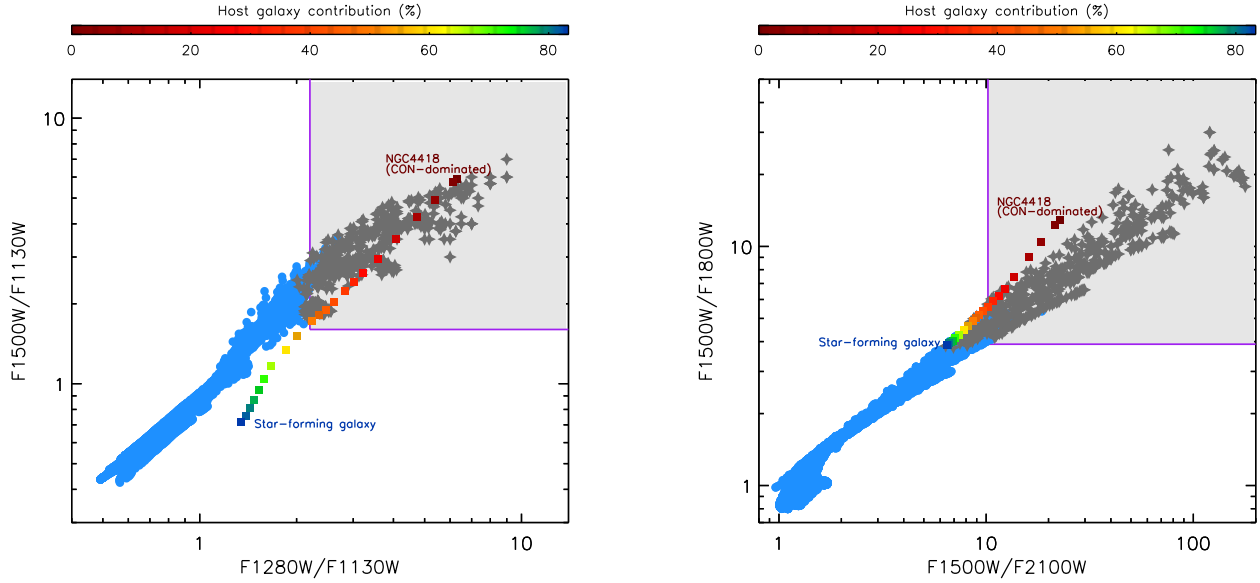


Fig. 10. Colour-colour diagrams using JWST filters. *Left panel:* smooth CYGNUS torus model SEDs at $z = 0$. *Right panel:* smooth CYGNUS torus model SEDs at $z = 1$. Blue circles correspond to the broad-band filter ratio for all the SEDs of smooth CYGNUS torus models. Grey stars represent those ratios of the model SEDs of deeply obscured nuclei (classified based on the continuum ratio criteria presented in Sect. 5). The purple square denotes the region where CON-dominated sources are located (see Sect. 6). Colour-coded squares correspond to the host galaxy contribution of the track of simulated spectra for a galaxy containing a CON shown in Fig. 5.

geometry and a smooth dust distribution. This suggests that the nuclear dusty structure of deeply obscured galaxy nuclei has an extremely high dust coverage.

7. We find that the use of mid-IR colour-colour diagrams is an effective method to select CON-dominated sources at different redshifts. In particular, the combination of filters of the JWST/MIRI will enable the selection of CONs out to $z \sim 1.5$. This will allow the selection of CONs to be extended to high redshifts where U/LIRGs are more numerous.

The high spatial resolution (improvement by a factor of ten in spatial resolution with respect to *Spitzer*/IRS) and unprecedented sensitivity that will be afforded by the JWST will allow observations of distant and faint galaxies containing CONs. In the future, Origins Space Telescope-like missions will provide the high sensitivity and IR spectral coverage needed to extrapolate our mid-IR colour-colour technique to identify CONs amongst more distant galaxy populations.

Acknowledgements. I.G.B. and D.R. acknowledge support from STFC through grant ST/S000488/1. D.R. also acknowledges support from the University of Oxford John Fell Fund. The authors thank Almudena Alonso-Herrero and Miguel Pereira-Santaella for discussions, and Jason Marshall for providing the galaxy disk template spectrum. This work is based [in part] on archival data obtained with the *Spitzer* Space Telescope, which is operated by the Jet Propulsion Laboratory, California Institute of Technology under a contract with NASA. This research has also made use of the NASA/IPAC Extragalactic Database (NED), which is operated by the Jet Propulsion Laboratory, California Institute of Technology under a contract with NASA. Finally, we thank the anonymous referee for their useful comments.

References

Aalto, S., Martín, S., Costagliola, F., et al. 2015, *A&A*, **584**, A42
Aalto, S., Müller, S., König, S., et al. 2019, *A&A*, **627**, A147
Allamandola, L. J., Tielens, A. G. G. M., & Barker, J. R. 1989, *ApJS*, **71**, 733
Alonso-Herrero, A., Ramos Almeida, C., Esquej, P., et al. 2014, *MNRAS*, **443**, 2766
Alonso-Herrero, A., Esquej, P., Roche, P. F., et al. 2016, *MNRAS*, **455**, 563
Alonso-Herrero, A., Pereira-Santaella, M., Rigopoulou, D., et al. 2020, *A&A*, **639**, A43

Armus, L., Charmandaris, V., Bernard-Salas, J., et al. 2007, *ApJ*, **656**, 148
Armus, L., Mazzarella, J. M., Evans, A. S., et al. 2009, *PASP*, **121**, 559
Brandl, B. R., Bernard-Salas, J., Spoon, H. W. W., et al. 2006, *ApJ*, **653**, 1129
Boogert, A. C. A., Pontoppidan, K. M., Knez, C., et al. 2008, *ApJ*, **678**, 985
Boogert, A. C. A., Huard, T. L., Cook, A. M., et al. 2011, *ApJ*, **729**, 92
Desai, V., Armus, L., Spoon, H. W. W., et al. 2007, *ApJ*, **669**, 810
Díaz-Santos, T., Alonso-Herrero, A., Colina, L., et al. 2008, *ApJ*, **685**, 211
Díaz-Santos, T., Charmandaris, V., Armus, L., et al. 2010, *ApJ*, **723**, 993
Efstathiou, A., & Rowan-Robinson, M. 1995, *MNRAS*, **273**, 649
Efstathiou, A., Farrah, D., Afonso, J., et al. 2021, *MNRAS*, **512**, 5183
Esquej, P., Alonso-Herrero, A., González-Martín, O., et al. 2014, *ApJ*, **780**, 86
Falstad, N., Hallqvist, F., Aalto, S., et al. 2019, *A&A*, **623**, A29
Falstad, N., Aalto, S., König, S., et al. 2021, *A&A*, **649**, A105
Farrah, D., Lonsdale, C. J., Weedman, D. W., et al. 2008, *ApJ*, **677**, 957
Farrah, D., Leboutteiller, V., Spoon, H. W. W., et al. 2013, *ApJ*, **776**, 38
García-Bernete, I., Rigopoulou, D., Alonso-Herrero, A., et al. 2022, *MNRAS*, **509**, 4256
Georgantopoulos, I., Dasyra, K. M., Rovilos, E., et al. 2011, *A&A*, **531**, A116
González-Martín, O., Rodríguez-Espinosa, J. M., Díaz-Santos, T., et al. 2013, *A&A*, **553**, A35
Goulding, A. D., Alexander, D. M., Bauer, F. E., et al. 2012, *ApJ*, **755**, 5
Helou, G., & Walker, D. W. 1986, *The IRAS Point Source Catalog v2.1 (PSC)*, <https://irsa.ipac.caltech.edu/IRASdocs/surveys/psc.html>
Hatziminaoglou, E., Hernán-Caballero, A., Feltre, A., & Piñol, Ferrer N. 2015, *ApJ*, **803**, 110
Hernán-Caballero, A., & Hatziminaoglou, E. 2011, *MNRAS*, **414**, 500
Hernán-Caballero, A., Pérez-Fournon, I., Hatziminaoglou, E., et al. 2009, *MNRAS*, **395**, 1695
Hernán-Caballero, A., Spoon, H. W. W., Leboutteiller, V., Rupke, D. S. N., & Barry, D. P. 2016, *MNRAS*, **455**, 1796
Hernán-Caballero, A., Spoon, H. W. W., Alonso-Herrero, A., et al. 2020, *MNRAS*, **497**, 4614
Herrero-Illana, R., Pérez-Torres, M. Á., Randriamanakoto, Z., et al. 2017, *MNRAS*, **471**, 1634
Hönig, S. F., Kishimoto, M., Gandhi, P., et al. 2010, *A&A*, **515**, A23
Houck, J. R., Roellig, T. L., van Cleve, J., et al. 2004, *ApJS*, **154**, 18
Imanishi, M., & Nakanishi, K. 2013, *AJ*, **146**, 91
Imanishi, M., Dudley, C. C., Maiolino, R., et al. 2007, *ApJS*, **171**, 72
Jensen, J. J., Hönig, S. F., Rakshit, S., et al. 2017, *MNRAS*, **470**, 3071
Kaneda, H., Onaka, T., Sakon, I., et al. 2008, *ApJ*, **684**, 270
Kormendy, J., & Ho, L. C. 2013, *ARA&A*, **51**, 511
Leboutteiller, V., Barry, D. J., Spoon, H. W. W., et al. 2011, *ApJS*, **196**, 8
Leger, A., & Puget, J. L. 1984, *A&A*, **137**, L5
Levenson, N. A., Sirocky, M. M., Hao, L., et al. 2007, *ApJ*, **654**, L45

- Li, A. 2020, [NatAs](#), **4**, 339
- Lutz, D., Spoon, H. W. W., Rigopoulou, D., Moorwood, A. F. M., & Genzel, R. 1998, [ApJ](#), **505**, L103
- Marshall, J. A., Elitzur, M., Armus, L., Diaz-Santos, T., & Charmandaris, V. 2018, [ApJ](#), **858**, 59
- Mateos, S., Alonso-Herrero, A., Carrera, F. J., et al. 2013, [MNRAS](#), **434**, 941
- Ossenkopf, V., Henning, T., & Mathis, J. S. 1992, [A&A](#), **261**, 567
- Pearson, C., Rigopoulou, D., Hurley, P., et al. 2016, [ApJS](#), **227**, 9
- Peeters, E., Spoon, H. W. W., & Tielens, A. G. G. M. 2004, [ApJ](#), **613**, 986
- Pilbratt, G. L., Riedinger, J. R., Passvogel, T., et al. 2010, [A&A](#), **518**, L1
- Pope, A., Chary, R.-R., Alexander, D. M., et al. 2008, [ApJ](#), **675**, 1171
- Rigopoulou, D., Spoon, H. W. W., Genzel, R., et al. 1999, [AJ](#), **118**, 2625
- Rigopoulou, D., Kunze, D., Lutz, D., Genzel, R., & Moorwood, A. F. M. 2002, [A&A](#), **389**, 374
- Roche, P. F., Aitken, D. K., Smith, C. H., & Ward, M. J. 1991, [MNRAS](#), **248**, 606
- Roche, P. F., Alonso-Herrero, A., & Gonzalez-Martin, O. 2015, [MNRAS](#), **449**, 2598
- Sajina, A., Yan, L., Lacy, M., & Huynh, M. 2007, [ApJ](#), **667**, L17
- Sajina, A., Spoon, H., Yan, L., et al. 2009, [ApJ](#), **703**, 270
- Sakamoto, K., Aalto, S., Costagliola, F., et al. 2013, [ApJ](#), **764**, 42
- Sakamoto, K., Aalto, S., Evans, A. S., Wiedner, M. C., & Wilner, D. J. 2010, [ApJ](#), **725**, L228
- Sakamoto, K., Aalto, S., Barcos-Muñoz, L., et al. 2017, [ApJ](#), **849**, 14
- Sanders, D. B., Mazzarella, J. M., Kim, D.-C., Surace, J. A., & Soifer, B. T. 2003, [AJ](#), **126**, 1607
- Scoville, N., Murchikova, L., Walter, F., et al. 2017, [ApJ](#), **836**, 66
- Shipley, H. V., Papovich, C., Rieke, G. H., Brown, M. J. I., & Moustakas, J. 2016, [ApJ](#), **818**, 60
- Siebenmorgen, R., Krügel, E., Spoon, H. W. W., et al. 2004, [A&A](#), **414**, 123
- Sirocky, M. M., Levenson, N. A., Elitzur, M., Spoon, H. W. W., & Armus, L. 2008, [ApJ](#), **678**, 729
- Smith, C. H., Aitken, D. K., & Roche, P. F. 1989, [MNRAS](#), **241**, 425
- Smith, J. D. T., Draine, B. T., Dale, D. A., et al. 2007, [ApJ](#), **656**, 770
- Spoon, H. W. W., Marshall, J. A., Houck, J. R., et al. 2007, [ApJ](#), **654**, L49
- Spoon, H. W. W., Hernán-Caballero, A., Rupke, D., et al. 2022, [ApJS](#), **259**, 37
- Stern, D., Assef, R. J., Benford, D. J., et al. 2012, [ApJ](#), **753**, 30
- Stierwalt, S., Armus, L., Surace, J. A., et al. 2013, [ApJS](#), **206**, 1
- Tielens, A. G. G. M. 2008, [ARA&A](#), **46**, 289
- Veilleux, S., Rupke, D. S. N., Kim, D.-C., et al. 2009, [ApJS](#), **182**, 628
- Voit, G. M. 1992, [MNRAS](#), **258**, 841

Appendix A: Fraction of the galaxy covered by Spitzer/IRS

Here we investigate the fraction of the galaxy integrated mid-IR emission that is measured by Spitzer/IRS. We note that the area of the galaxy covered by the slit of Spitzer/IRS depends on the particular size of the galaxy and its distance. To do so, we retrieve $12\mu\text{m}$ IRAS fluxes from the Infrared Astronomical Satellite (IRAS) Revised Bright Galaxy Sample (RBGS; Sanders et al. 2003) and the IRAS Point Source Catalog³ (IRAS PSC; Helou & Walker 1986). We note that IRAS data were obtained with a 0.6-m telescope with a pixel size of $2'$ and an angular resolution of $\sim 4'$. Therefore, the fluxes measured within the large IRAS apertures are representative of the integrated properties of the galaxies. Using the IRAS and Spitzer/IRS flux ratio at $12\mu\text{m}$, we can estimate the fraction of the total galaxy mid-IR emission measured by Spitzer/IRS.

Figure A.1 shows that the classification of group 1 and 2 of ULIRGs does not depend on the fraction of the total galaxy measured by Spitzer/IRS. We find that ULIRGs tend to have smaller IRAS $12\mu\text{m}$ /IRS $12\mu\text{m}$ flux ratios (average value of 1.32 ± 0.39 and 1.13 ± 0.27 for the HERUS and GOALS ULIRGs, respectively) than LIRGs (average value of 5.11 ± 12.79 for the GOAL LIRGs). This is in agreement with previous works (e.g., Díaz-Santos et al. 2010) which showed that the mid-IR continuum emitting regions of ULIRGs are compact and less than 30% of their mid-IR emission is extended. However, LIRGs are not as compact as ULIRGs on average (e.g. Díaz-Santos et al. 2008, Díaz-Santos et al. 2010).

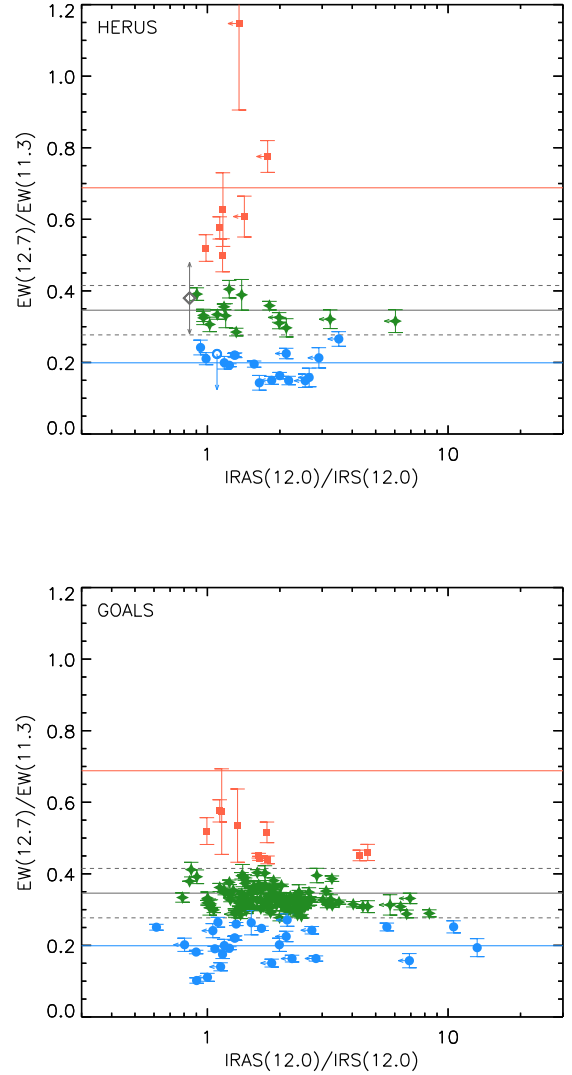


Fig. A.1. *Top panel:* $12.7/11.3\mu\text{m}$ PAH EW ratio vs the IRAS $12\mu\text{m}$ /IRS $12\mu\text{m}$ flux ratios for the HERUS sample. Green, blue, and red symbols correspond to group 1, 2, and 3 of sources (see Sect. 4.1). *Bottom panel:* same as the top panel but using the GOALS sample. The grey solid and dashed horizontal lines correspond to the average and 3σ values found by Hernán-Caballero et al. (2020) for star-forming galaxies. The blue and red solid horizontal lines represent the average values found for groups 2 and 3 of ULIRGs (see Sect. 4.1).

³ <https://irsa.ipac.caltech.edu/IRASdocs/surveys/psc.html>